

Chapter 3

Molecular Simulation

3.1 Introduction

In the previous chapter it was shown that the prediction of the properties of a molecular liquid was a complex many body problem, impossible to solve directly using analytic techniques. This led to the use of statistical mechanics or microscopic models such as the Doi-Edwards model to obtain constitutive equations for polymer melts. In Section 2.5.2 of the last chapter we have introduced some of the coarse-grained simulation techniques which have evolved from this model. In this chapter and indeed for the remainder of the thesis we will deal with molecular dynamics simulations, in particular nonequilibrium molecular dynamics simulations (NEMD) of systems under PCF and PEF. These rigorous methods derive their strength from nonequilibrium statistical mechanics and in particular nonlinear response theory [EM90]. There are two aims of this chapter: Firstly we give details and some background to the molecular simulations that we use in the remainder of the thesis and secondly we show the connection between the Kraynik-Reinelt technique for the simulation of planar extensional flow and the Arnold cat map, a well known prototype for a dynamical system. We intend to give just a summary of the molecular dynamics techniques

used, referring the reader to the relevant literature for further detail. At this point we cite some general reviews of the NEMD techniques including: Todd and Daivis [TD07]; Sarman, Evans and Cummings [SEC98] and the book by Evans and Morriss [EM90]. A separate review of the molecular dynamics literature specific to the topics of following chapters is given at the beginning of the relevant chapter.

The NEMD techniques that we use in this thesis are some of the broader range of molecular simulation methods. Here we briefly discuss Monte Carlo simulations and equilibrium molecular dynamic techniques.

The Monte Carlo technique, which has its origin in the Metropolis algorithm [MRR⁺53], seeks to efficiently calculate ensemble averages of a model system based on the underlying distribution known from statistical mechanics. In its application to polymeric systems, an intermolecular potential for the system of molecules is chosen and then a collection of algorithms is used to sample the chosen ensemble. For polymeric systems several specialised algorithms have been developed. Here we cite the *configurational bias* algorithms [dPLS92, SF92], and the *end bridging* [PT95] and *generalised bridging* [Uhl00] algorithms which allow the efficient simulation of polydisperse as well as monodisperse systems [KGMT02] of linear and branched polymers [KMT02]. There has been some exploration of the use of Monte Carlo simulations for calculating nonequilibrium properties [MT98, MÖ02]. However, the main use of Monte Carlo techniques has been for equilibrium systems.

Equilibrium molecular dynamics simulations (MD), as we will explain briefly again below, begin with a chosen molecular potential to model the system. In most cases the equations of motion used are deterministic coupled ordinary differential equations chosen according to the statistical ensemble studied. For example to simulate a system in the canonical ensemble the Nosé-Hoover algorithm is used. Equilibrium molecular dynamics is used in cases where information about the time dependent dynamics, rather than

just the configuration, is desired. The most common example of this is the calculation of the diffusion coefficient where the time dependence of the mean-squared displacement of atoms or molecules is required. We will discuss this application at length in Chapter 5. Further equilibrium transport coefficients such as the zero strain-rate viscosity or the thermal conductivity may be calculated using the relevant Green-Kubo expressions. Examples of the use of equilibrium molecular dynamics simulations for polymeric liquids include the work of Paul *et al.* [PSY97, PSYF98, PF99] and Harmandaris *et al.* [HMT00, HMT⁺02]. In both of these groups of works dynamical properties of chain molecules are compared to the predictions of the Rouse model. In the works of Harmandaris *et al.* Monte Carlo simulations were used to efficiently produce equilibrated systems. Kremer and Grest [KG90] have performed simulations at equilibrium with a Brownian dynamics algorithm [GK86] with many aspects similar to deterministic equilibrium MD. However, each particle is coupled weakly to a heat bath via a random force which makes the algorithm nondeterministic. Several subsequent works have used this algorithm to simulate polymeric liquids [TKB⁺98, TKH⁺98, Fal00, AEG⁺03, ESG⁺04].

3.2 Equations of motion and thermostats: atomic systems

In a MD simulation the time evolution of the positions and momenta of the particles are calculated. Hamilton's equations of motion for a system of particles in the microcanonical ensemble [Hua87, McQ76] would be,

$$\begin{aligned}\dot{\mathbf{r}}_i &= \frac{\mathbf{p}_i}{m_i} \\ \dot{\mathbf{p}}_i &= \mathbf{F}_i\end{aligned}\tag{3.1}$$

where \mathbf{r}_i (\mathbf{p}_i) are the position (momentum) of particle i , \mathbf{F}_i is the force on particle i due to the other particles and m_i is the mass of particle i . For a system of N point particles with no internal degrees of freedom the ‘*Atomic*’ temperature T_A of the system is determined from the equipartition theorem [Hua87] to be,

$$T_A = \left\langle \frac{2}{(3N - f)k_B} \sum_{i=1}^N \left(\frac{\mathbf{p}_i^2}{2m_i} \right) \right\rangle. \quad (3.2)$$

Here k_B is Boltzmann’s constant, the angled brackets $\langle \dots \rangle$ denote an ensemble average and f is the number of degrees of freedom lost through constraints. If we want to simulate the system at constant temperature, *i.e.* in the isokinetic ensemble, it is sufficient to constrain the kinetic energy of the system, consequently T_A is also fixed at a constant value. This becomes a constraint to Hamilton’s equations (3.1). By introducing a thermostating term into (3.1) the equations become,

$$\begin{aligned} \dot{\mathbf{r}}_i &= \frac{\mathbf{p}_i}{m_i}, \\ \dot{\mathbf{p}}_i &= \mathbf{F}_i - \zeta_A \mathbf{p}_i \end{aligned} \quad (3.3)$$

ζ_A is the ‘*Atomic*’ thermostat multiplier [EM90]. The value of ζ_A is determined by noting that the instantaneous time derivative of T_A vanishes, consequently,

$$\begin{aligned} \frac{dT_A}{dt} &= \frac{1}{(3N - f)k_B} \frac{d}{dt} \sum_{i=1}^N \mathbf{p}_i \cdot \mathbf{p}_i \\ &= \frac{2}{(3N - f)k_B} \sum_{i=1}^N \dot{\mathbf{p}}_i \cdot \mathbf{p}_i \\ &= \frac{2}{(3N - f)k_B} \sum_{i=1}^N (\mathbf{F}_i - \zeta_A \mathbf{p}_i) \cdot \mathbf{p}_i = 0. \end{aligned}$$

The last line here may be rearranged to give the thermostat multiplier,

$$\zeta_A = \frac{\sum_{i=1}^N \mathbf{F}_i \cdot \mathbf{p}_i}{\sum_{i=1}^N \mathbf{p}_i^2}. \quad (3.4)$$

A system of particles under these equations of motion simulate the *isokinetic* ensemble. To simulate the canonical ensemble one can use the Nosé-Hoover algorithm [Nos84b, Nos84a, Hoo85]. In addition to the equations of motion, suitable boundary conditions are required for MD simulations. This topic is left until Section 3.6 where it is discussed in significant detail.

To simulate systems under flow a mechanism is required which imposes a velocity profile on the fluid. In the case of PCF one technique for achieving this involves the simulation of fluid particles confined between two solid walls composed of atoms [LBC92], in which the lower wall remains fixed in space and the upper wall moves at a constant velocity in the direction of shear, resulting in a uniform velocity profile in the fluid. By thermostating the two walls the system can be kept at a constant temperature for small shear rates. However, at large shear rates the increase in internal energy cannot be compensated for by thermostating just the walls and a temperature gradient results. Furthermore, the structure of the walls induces density gradients in the fluid such that the fluid is not spatially homogeneous. Both these reasons make such simulations problematic in understanding the transport processes of spatially homogeneous systems at constant temperature. In particular the system cannot be analysed using response theory.

To avoid these problems, methods have been developed which apply an external field to the system of particles. Together with suitable boundary conditions (see Section 3.6) this results in the simulation of homogeneous flows. Of these methods, the most widely used has been the SLLOD algorithm [EHH84, EHF⁺83, EM90]. The equations of motion of this algorithm

for atomic systems are,

$$\begin{aligned}\dot{\mathbf{r}}_i &= \frac{\mathbf{P}_i}{m_i} + \mathbf{r}_i \cdot \nabla \mathbf{u} \\ \dot{\mathbf{p}}_i &= \mathbf{F}_i - \mathbf{p}_i \cdot \nabla \mathbf{u} - \zeta_A \mathbf{p}_i.\end{aligned}\quad (3.5)$$

Comparing these with Hamilton's equations (3.1), both the momentum and position equations are augmented by terms linear in the velocity gradient $\nabla \mathbf{u}$. An expression for the thermostat ζ_A is derived in a similar way to (3.4) and is found to be,

$$\zeta_A = \frac{\sum_{i=1}^N (\mathbf{F}_i \cdot \mathbf{p}_i - \mathbf{p}_i \cdot \nabla \mathbf{u} \cdot \mathbf{p}_i)}{\sum_{i=1}^N \mathbf{p}_i^2}\quad (3.6)$$

The momenta here (\mathbf{p}_i) do not contain the streaming velocity component \mathbf{u} ; here we will call them the peculiar momenta although they can also be referred to as the thermal momenta. Both the equations of motion and the thermostat ((3.5) and (3.6)) are equivalent to their equilibrium counterparts ((3.3) and (3.4)) when $\nabla \mathbf{u} = 0$. Full details of the derivation and validity of the SLLOD equations for PCF are given in the book by Evans and Morriss [EM90]. The derivation of the SLLOD algorithm for general homogeneous flows (including PEF) has been published by Daivis and Todd [DT06].

The SLLOD equations of motion for a system of atoms undergoing isothermal PCF are

$$\dot{\mathbf{r}}_i = \frac{\mathbf{P}_i}{m_i} + \dot{\gamma} y_i \hat{\mathbf{n}}_x \quad (3.7)$$

$$\dot{\mathbf{p}}_i = \mathbf{F}_i - \dot{\gamma} p_{iy} \hat{\mathbf{n}}_x - \zeta_A \mathbf{p}_i \quad (3.8)$$

where $\mathbf{r}_i = (x_i, y_i, z_i)$ is the laboratory position of atom i with peculiar (*i.e.* thermal) momentum $\mathbf{p}_i = (p_{ix}, p_{iy}, p_{iz})$ and mass m_i . $\dot{\gamma}$ is the shear rate for the system being simulated. The force on atom i due to the surrounding atoms is \mathbf{F}_i and is dependent on the chemical nature of the system, while

ζ_A is an atomic thermostat that may be given in the Gaussian form [EM90] by

$$\zeta_A = \frac{\sum_{i=1}^N (\mathbf{F}_i \cdot \mathbf{p}_i) - \dot{\gamma} p_{ix} p_{iy}}{\sum_{i=1}^N \mathbf{p}_i^2}. \quad (3.9)$$

The corresponding SLLOD equations of motion for PEF are [TD98, TD99]

$$\dot{\mathbf{r}}_i = \frac{\mathbf{p}_i}{m_i} + \dot{\epsilon}(x_i \hat{\mathbf{n}}_x - y_i \hat{\mathbf{n}}_y), \quad (3.10)$$

$$\dot{\mathbf{p}}_i = \mathbf{F}_i - \dot{\epsilon}(p_{xi} \hat{\mathbf{n}}_x - p_{yi} \hat{\mathbf{n}}_y) - \zeta_A \mathbf{p}_i \quad (3.11)$$

The Gaussian thermostat in this case is given by

$$\zeta_A = \frac{\sum_{i=1}^N (\mathbf{F}_i \cdot \mathbf{p}_i - \dot{\epsilon}(p_{ix}^2 - p_{iy}^2))}{\sum_{i=1}^N \mathbf{p}_i^2}. \quad (3.12)$$

3.3 Intermolecular potentials

The system is made to model a specific material with a suitable choice of intermolecular force \mathbf{F} that appears in all equations of motion in the last section. The force on atom i , \mathbf{F}_i , can be related to the potential energy of the whole system $U(\mathbf{r}_1, \mathbf{r}_2, \dots, \mathbf{r}_N)$ by the equation

$$\mathbf{F}_i = -\nabla_i U(\mathbf{r}_1, \mathbf{r}_2, \dots, \mathbf{r}_N) \quad (3.13)$$

Where ∇_i is defined as $\nabla_i = \left(\frac{\partial}{\partial r_{ix}}, \frac{\partial}{\partial r_{iy}}, \frac{\partial}{\partial r_{iz}} \right)$ if we use normal Cartesian coordinates ($\mathbf{r}_i = (r_{ix}, r_{iy}, r_{iz})$). The intermolecular potential can be expanded and grouped into terms dependent on single particles, pairs, triplets *etc.*,

$$U = \sum_i U_1(\mathbf{r}_i) + \sum_i \sum_{j>i} U_2(\mathbf{r}_i, \mathbf{r}_j) + \sum_i \sum_{j>i} \sum_{k>j>i} U_3(\mathbf{r}_i, \mathbf{r}_j, \mathbf{r}_k) + \dots \quad (3.14)$$

Here the potentials U_i are terms dependent on i particles. In many cases the system's potential can be decomposed as a sum of pair potentials. In cases

where there is no external field the first term vanishes. Third and fourth order terms U_3 and U_4 are often used in molecular potentials as bond angle potentials, described further in the next section.

A fundamental approximation made in classical molecular dynamics is that one ignores explicit quantum effects and chooses an intermolecular potential which gives a sufficiently good approximation to these effects. If this approximation could not be made and significant quantum effects existed in the system then a quantum molecular dynamics scheme would perhaps be necessary [CP85].

Two very common interatomic potentials are the Lennard-Jones (LJ) potential and the Weeks-Chandler-Anderson potential (WCA) [WCA71]. Both potentials are isotropic ($U(\mathbf{r}_i, \mathbf{r}_j) = U(|\mathbf{r}_j - \mathbf{r}_i|) \equiv U(r_{ij})$) and the full LJ potential shown in Fig. 3.1 has the following form,

$$U_{ij}^{LJ}(r_{ij}) = 4\epsilon_{LJ} \left[\left(\frac{\sigma_{LJ}}{r_{ij}} \right)^{12} - \left(\frac{\sigma_{LJ}}{r_{ij}} \right)^6 \right] \quad (3.15)$$

where σ_{LJ} and ϵ_{LJ} are the effective atomic diameter and well depth respectively. The WCA potential is essentially the repulsive part of the LJ potential and consequently has a cutoff radius at the LJ minimum $r_c = 2^{1/6}\sigma_{LJ}$.

$$U_{ij}^{WCA}(r_{ij}) = \begin{cases} 4\epsilon_{LJ} \left[\left(\frac{\sigma_{LJ}}{r_{ij}} \right)^{12} - \left(\frac{\sigma_{LJ}}{r_{ij}} \right)^6 \right] - U_c & \text{for } r_{ij} \leq r_c \text{ and} \\ 0 & \text{for } r_{ij} \geq r_c \end{cases} \quad (3.16)$$

where $U_c = U_{ij}^{LJ}(r_c)$. The WCA potential is shown in Fig. 3.2, together with the FENE potential which is used for molecular bonding discussed in the next section.

3.3.1 Molecular Models

One of the challenges for polymer simulation is the complexity of the material from a chemical point of view. We have already seen in the last chapter

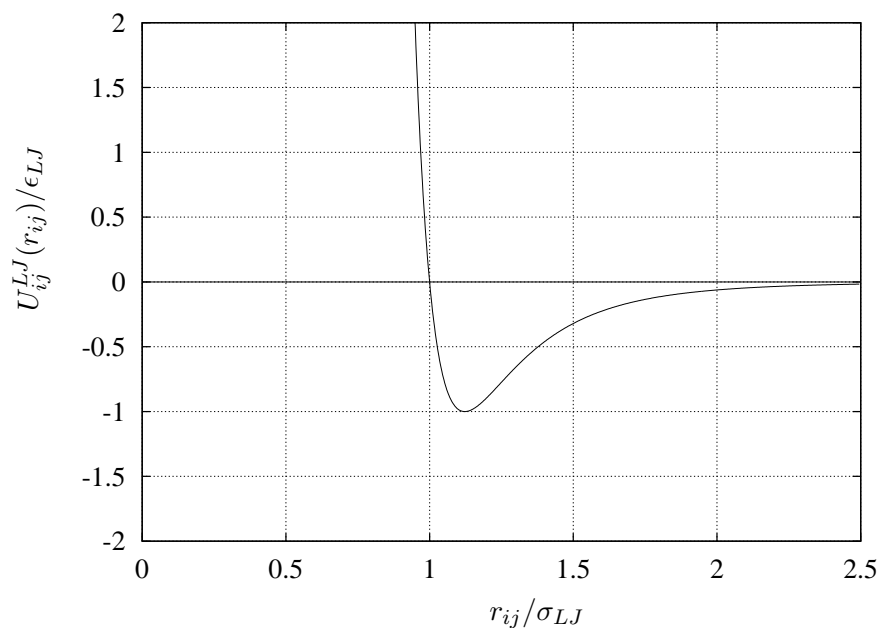


Figure 3.1: The Lennard-Jones potential. This potential is repulsive for $r_{ij}/\sigma_{LJ} < 2^{1/6}\sigma_{LJ}$ and attractive for $r_{ij}/\sigma_{LJ} > 2^{1/6}$. There is a minimum in the potential at $r_{ij} = 2^{1/6}\sigma_{LJ}$.

that modelling of these materials requires some degree of coarse-graining for results to be obtained. The situation is very similar for molecular simulation. From the outset it is theoretically possible to simulate polymer liquids from a fully atomistic point of view, where each atom in the real system is explicitly included in the simulated system. However, this approach is extremely demanding on computational resources and so is almost impossible from a practical point of view at present. To avoid this practical limitation, molecular models have been developed which reduce the number of degrees of freedom in the system by combining groups of bonded atoms together into coarse-grained particles. For example, in the united atom models of hydrocarbons (see for example [MGWP98, UBD⁺00]), CH_2 and CH_3 groups are considered as a single bead or united atom which is represented with a LJ-potential and bonding between carbon atoms is represented by bending and torsional potentials. The parameters of the torsional potential are cho-

sen to fit the bond properties, particularly the preferred rotational states that we described in Section 2.4. Works which have used this type of potential include several of the equilibrium MD and Monte Carlo works described above.

A systematic process of selecting a coarse-grained model for an MD simulation is a difficult undertaking. We mention the significant work of Baschnagel *et al.* [BBD⁺00] in which the coarse-graining process is examined at several different scales and with a number of different methods.

In this work we have chosen to compare the calculated rheological properties of two molecular models which incorporate less atomic detail than described in the models above. The models we compare are the *freely jointed chain* (FJC) model and the *finitely extensible non-linear elastic* (FENE) model. This is the main topic of the next chapter and so at this stage just the most important algorithmic details are provided. A schematic diagram of each molecule is given in Fig. 3.3: The FENE molecule consists of beads connected by flexible bonds. The FJC model consists of beads connected by bonds with a fixed length.

The FENE molecule

The FENE molecules that we simulate here consist of a linear chain of N_s beads interacting via pair potentials. Adjacent beads along the chain interact via a combined FENE spring potential and WCA potential. Beads which are not on the same molecule and beads which *are* on the same molecule but not adjacent interact just by the WCA potential (3.16). For two adjacent beads separated by the vector \mathbf{r}_{ij} , the FENE contribution to their interaction is,

$$U_{ij}^{FENE} = \begin{cases} -\frac{1}{2}kR_0^2 \log_e \left[1 - \left(\frac{r_{ij}}{R_0} \right)^2 \right] & \text{for } r_{ij} \leq R_0 \text{ and} \\ +\infty & \text{for } r_{ij} \geq R_0 \end{cases} \quad (3.17)$$

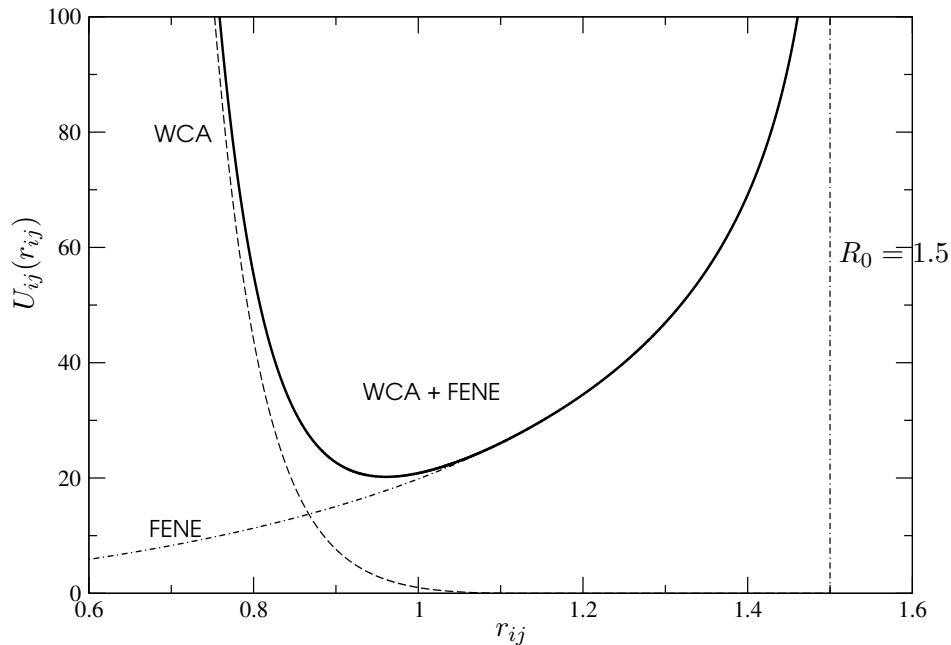


Figure 3.2: A comparison of the FENE and WCA potentials, and their sum

Where $k = 30\epsilon_{LJ}$ is the spring constant for the FENE bond (in a similar way to the Hookean spring constant), $R_0 = 1.5\sigma_{LJ}$ is the limit to the bond extension (see Fig. 3.2), and $r_{ij} = |\mathbf{r}_j - \mathbf{r}_i|$ is the distance between particles i and j . The importance of the FENE potential over a Hookean potential is that a FENE bond cannot be extended beyond the fixed length $R_0 = 1.5\sigma_{LJ}$. A plot of the potential between adjacent beads is given in Fig. 3.2. Note that the potential has a minimum close to $r_{ij} = 1.0\sigma_{LJ}$. The choice of coefficients k and R_0 are the values that have been used in a number of previous investigations using this potential [KLH93, KLM97, KH00, BTS04a, BTS04b, BTS05]. It has been reported by the authors in these works that the molecules did not cross each other. Thus a key property of the polymers was correctly modelled.

As we have just noted the FENE model described here has been used in several other works by Kröger *et al.* [KLH93, KLM97, KH00] for simulation of linear molecules and recently by Bosko *et al.* [BTS04a, BTS04b, BTS05]

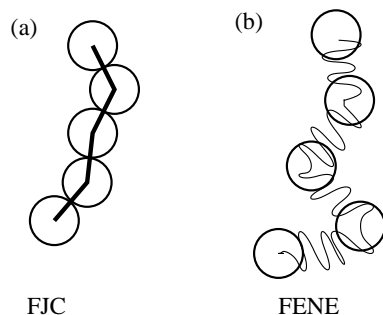


Figure 3.3: FENE and FJC molecules.

for simulation of dendritic branched molecules and comparison with linear molecules. Kröger and Hess [KH00] simulated systems of molecules up to $N_s = 400$ and were able to compare the systems with polyethylene and polystyrene melts by comparing structural properties of the melt with those from experiment.

The FJC molecule

We have also simulated linear molecules with constrained bond lengths. The Gaussian constraint method used to calculate the constraint force is presented in works by Edberg *et al.* [EEM86, EME87] and by Morriss and Evans [ME91]. In addition to the constraint force, the short ranged and repulsive WCA potential is imposed between atoms on different chains and between atoms on the same chain which are not adjacent. In previous works by Matin, Daivis and Todd [MDT00, MDT03, DMT03, DMT07] the bond length had been constrained to $b = 1.0\sigma_{LJ}$. In this work however, we have constrained the bond length to $b = 0.97\sigma_{LJ}$. This corresponds to the average of the bond length of the FENE molecule at equilibrium (for $T = 1.0$, $\rho = 0.84$). Further discussion of this choice of bond length is given in the next chapter.

We must note that the names we use for these models have been used

in the past to nominate other molecular models which differ from those used here. In particular, the term ‘freely-jointed-chain’ is commonly used to denote any model in which the bond angles are free to have any orientation. Furthermore, the FENE potential is commonly used to denote dimers and chains which just use the potential as given in (3.17) without the inclusion of the repulsive contribution from the WCA potential.

3.4 Equations of motion for molecular systems

The SLLOD equations of motion that we use here for molecular systems are given by:

$$\dot{\mathbf{r}}_{i\alpha} = \frac{\mathbf{p}_{i\alpha}}{m_{i\alpha}} + \mathbf{r}_i \cdot \nabla \mathbf{u} \quad (3.18)$$

$$\dot{\mathbf{p}}_{i\alpha} = \mathbf{F}_{i\alpha}^{LJ} + \mathbf{F}_{i\alpha}^{C/FENE} - \frac{m_{i\alpha}}{M_i} \mathbf{p}_i \cdot \nabla \mathbf{u} - \zeta_M \frac{m_{i\alpha}}{M_i} \mathbf{p}_i \quad (3.19)$$

This is the so-called ‘molecular SLLOD’ implementation. The subscript $i\alpha$ denotes site α on molecule i . $\mathbf{r}_{i\alpha}$, $(\mathbf{p}_{i\alpha}, m_{i\alpha})$ is the position (momentum, mass) of the designated site. The force on a site is separated into two terms; $\mathbf{F}_{i\alpha}^{LJ}$ is the contribution due to the Lennard-Jones interaction and $\mathbf{F}_{i\alpha}^{C/FENE}$ is either the constraint force for a FJC system or the bonding force for the FENE system. M_i is the mass of molecule i , and ζ_M is the molecular thermostat multiplier. $\mathbf{r}_i = (r_{xi}, r_{yi}, r_{zi})$ and $\mathbf{p}_i = (p_{xi}, p_{yi}, p_{zi})$ are the centre of mass and momentum of molecule i , given as:

$$\mathbf{r}_i = \frac{\sum_{\alpha=1}^{N_s} m_{i\alpha} \mathbf{r}_{i\alpha}}{\sum_{\alpha=1}^{N_s} m_{i\alpha}} \quad (3.20)$$

$$\mathbf{p}_i = \sum_{\alpha=1}^{N_s} \mathbf{p}_{i\alpha} \quad (3.21)$$

and the molecular thermostat is

$$\zeta_M = \frac{\sum_{i=1}^{N_m} (\mathbf{F}_i \cdot \mathbf{p}_i - \mathbf{p}_i \cdot \nabla \mathbf{u} \cdot \mathbf{p}_i) / M_i}{\sum_{i=1}^{N_m} \mathbf{p}_i^2 / M_i} \quad (3.22)$$

The streaming component of a site's velocity is determined at the centre of mass of the molecule, as opposed to the streaming-velocity at the site. For PCF these equations are,

$$\dot{\mathbf{r}}_{i\alpha} = \frac{\mathbf{p}_{i\alpha}}{m_{i\alpha}} + r_{yi} \hat{\mathbf{n}}_x \dot{\gamma} \quad (3.23)$$

$$\dot{\mathbf{p}}_{i\alpha} = \mathbf{F}_{i\alpha}^{LJ} + \mathbf{F}_{i\alpha}^{C/FENE} - \frac{m_{i\alpha}}{M_i} \hat{\mathbf{n}}_x \dot{\gamma} p_{yi} - \zeta_M \frac{m_{i\alpha}}{M_i} \mathbf{p}_i. \quad (3.24)$$

While for PEF the equations are,

$$\dot{\mathbf{r}}_{i\alpha} = \frac{\mathbf{p}_{i\alpha}}{m_{i\alpha}} + (r_{xi} \hat{\mathbf{n}}_x - r_{yi} \hat{\mathbf{n}}_y) \dot{\epsilon} \quad (3.25)$$

$$\dot{\mathbf{p}}_{i\alpha} = \mathbf{F}_{i\alpha}^{LJ} + \mathbf{F}_{i\alpha}^{C/FENE} - \frac{m_{i\alpha}}{M_i} (r_{xi} \hat{\mathbf{n}}_x - r_{yi} \hat{\mathbf{n}}_y) \dot{\epsilon} - \zeta_M \frac{m_{i\alpha}}{M_i} \mathbf{p}_i. \quad (3.26)$$

The combination of equations of motion and thermostat are collectively known as molecular SLLOD/molecular thermostat (MSMT). Our use of MSMT is the result of several investigations reported in the literature regarding the merits of different equations of motion and thermostats. For example, in the work of Padilla and Toxverd [PT96] it was shown that the results from atomic and molecular thermostated systems differed, but that results using the molecular thermostat were closer to those of a system which was thermostated by the surrounding fluid. Furthermore, in detailed investigations of Travis *et al.* [TDE95a, TDE95b, TE96], it was found that the use of atomic SLLOD together with an atomic thermostat for molecular fluids led to an antisymmetric component in the molecular pressure tensor (see Section 3.5) which imposed a torque on molecules as well as leading to excessive molecular alignment in the system. In contrast, it was found that this effect did not occur with the use of MSMT. One disadvantage of

MSMT, especially for large molecules, is that the thermostat only acts on a fraction of the degrees of freedom in the system. At high strain-rates this may result in the degrees of freedom that are not thermostated to overheat.

It has been suggested that possible improvement of algorithms for molecular systems may be found through the use of recently developed configurational thermostats. These thermostats which rely just on the positions of particles in the system make no assumptions about the streaming velocity of atoms within the fluid. However, the disadvantage persists that only a fraction of the degrees of freedom will be thermostated. The first example of a configurational thermostat was provided by Delhommelle and Evans [DE01, DE02] and Lue *et al.* [LJDE02] proposed a thermostat of the configurational temperature for molecular systems which has the advantage of being independent of the streaming velocity. Related work has continued and Braga and Travis [BT05] have developed a configurational thermostat algorithm which has several advantages over those of Delhommelle and Evans.

3.5 Calculation of Rheological and Energetic properties

To compare the results of NEMD simulations with experiment or with theory it is necessary to calculate macroscopic quantities. During the course of a simulation instantaneous values can be obtained and provided that the system is ergodic, accurate macroscopic predictions can be calculated. The pressure in a molecular liquid can be calculated using either of two expressions: the molecular or atomic pressure [EME87, TDE95a]. The molecular pressure is the pressure calculated using the intermolecular forces and the molecular centre of mass momenta. The instantaneous expression for the

molecular pressure is,

$$P_M V = \sum_{i=1}^{N_m} \frac{\mathbf{p}_i \mathbf{p}_i}{M_i} - \frac{1}{2} \sum_{i=1}^{N_m} \sum_{\alpha=1}^{N_s} \sum_{j \neq i}^{N_m} \sum_{\beta=1}^{N_s} \mathbf{r}_{ij} \mathbf{F}_{i\alpha j\beta}^{inter} \quad (3.27)$$

where \mathbf{r}_{ij} is the minimum image separation of the centres of mass of molecules i and j (explained in the following section on boundary conditions), $\mathbf{F}_{i\alpha j\beta}^{inter}$ is the interatomic force between site α on molecule i and site β on molecule j , \mathbf{p}_i is the momentum of the centre of mass of molecule i and V is the volume of the system. Note that in this case the second term, the virial, does not contain any intramolecular terms.

The atomic pressure on the other hand includes all atomic momenta and all interatomic forces and constraint forces. The expression for the atomic pressure is,

$$\begin{aligned} P_A V &= \sum_{i=1}^{N_m} \sum_{\alpha=1}^{N_s} \frac{\mathbf{p}_{i\alpha} \mathbf{p}_{i\alpha}}{m_{i\alpha}} - \frac{1}{2} \sum_{i=1}^{N_m} \sum_{\alpha=1}^{N_s} \sum_{j \neq i}^{N_m} \sum_{\beta=1}^{N_s} \mathbf{r}_{i\alpha j\beta} \mathbf{F}_{i\alpha j\beta} \\ &- \sum_{i=1}^{N_m} \sum_{\alpha=1}^{N_s-1} \sum_{\beta > \alpha}^{N_s} \mathbf{r}_{i\alpha j\beta} \mathbf{F}_{i\alpha j\beta} + \sum_{i=1}^{N_m} \sum_{\alpha=1}^{N_s} \mathbf{r}_{i\alpha} \mathbf{F}_{i\alpha}^C \end{aligned} \quad (3.28)$$

Here $\mathbf{r}_{i\alpha j\beta}$ is the vector between atom α on molecule i and atom β on molecule j , $\mathbf{F}_{i\alpha j\beta}$ is the corresponding interatomic force between these atoms.

As already noted above, Travis *et al.* [TDE95a, TDE95b, TE96] have investigated the differences between results using the molecular and atomic SLLOD algorithms under PCF. Included in these investigations was a comparison of molecular and atomic pressure tensors. The instantaneous atomic pressure tensor is symmetric since the forces involved act between centres of atoms. In the case of the instantaneous molecular pressure tensor the virial term is the dyadic product of the vector between the centres of mass of two molecules and the forces between atoms in the molecules. This is in general not a central force and gives rise to an antisymmetric component

of the instantaneous pressure tensor. However, it was found that the steady state averages of both the atomic and molecular stress tensors agreed, confirming the result of Edberg, Morriss and Evans [EME87]. From the steady state averages of the pressure tensor prediction of the viscosities and normal stresses can be calculated.

The instantaneous total internal energy of the system is given by,

$$U = \frac{1}{N_m} \left(\sum_{i=1}^{N_m} \sum_{\alpha=1}^{N_s} \frac{\mathbf{p}_{i\alpha}^2}{2m_{i\alpha}} + \sum_{i=1}^{N_m-1} \sum_{\alpha=1}^{N_s} \sum_{j=i+1}^{N_m} \sum_{\beta=1}^{N_s} U_{i\alpha j\beta} + \sum_{i=1}^{N_m} \sum_{\alpha=1}^{N_s-2} \sum_{\beta=\alpha+2}^{N_s} U_{i\alpha j\beta} \right). \quad (3.29)$$

In this expression the total energy of the system has been separated into its kinetic, intermolecular and intramolecular components. $U_{i\alpha j\beta}$ is the potential between atom α on molecule i and atom β on molecule j . As in the case of the pressure tensor a value to compare with experimental results is obtained by calculating a steady state average of the instantaneous value.

In the following two chapters we look at several other properties and they are introduced in detail as they are required. Here we simply summarise the properties that we investigate. The viscoelastic properties include the shear and extensional viscosities and the normal stress coefficients. Structural properties that we have investigated include the mean-squared end to end length of molecules $\langle \mathbf{R}_{ee}^2 \rangle$, and the mean-squared radius of gyration $\langle \mathbf{R}_G^2 \rangle$. For PCF we have also calculated the alignment angle of the end-to-end vector with the x -axis and the spin angular velocity of molecules ω_z which measures the average rate of rotation of molecules in the xy -plane. In Chapter 5 we investigate the diffusion of molecules in PCF and PEF. Out of equilibrium the diffusion coefficient becomes a second rank tensor. The properties we calculate in that chapter include velocity autocorrelation functions $C_{\alpha\beta}(t) = \langle v_\alpha(t)v_\beta(0) \rangle$ and the diffusion coefficients $D_{\alpha\beta}$, where α and β here range over the Cartesian coordinates.

3.6 Periodic boundary conditions

Simulations of atoms and molecules using the equations of motion described above require suitable boundary conditions that are compatible with the flow geometry. For the remainder of this chapter we discuss this topic, introducing the periodic boundary conditions (pbcs) that we use in our simulations and relating them to spatio-temporal maps from dynamical systems theory. Specifically, we show that the Kraynik-Reinelt pbcs used for simulations of PEF are related to the Arnold cat map from dynamical systems theory. For pedagogical purposes we first consider the relationship between maps and periodic boundary conditions at equilibrium and under PCF, as these two conditions are easier to understand.

3.6.1 Equilibrium

Simulation of atomistic systems without periodic boundary conditions are problematic because they are necessarily inhomogeneous at the boundary. This effect is only relevant if we are particularly interested in what happens at boundaries or interfaces. However, these effects obscure properties that are particular to the bulk of a fluid. We have limited this work to simulation of the bulk of the fluid. Doi-Edwards theory and the majority of constitutive models are specific to this case.

One way of reducing surface effects is by increasing the size of the system. Surface energies for example will scale with L^2 (L is the length scale of the simulation cell) while volume energies will scale with L^3 , so as L increases surface energies diminish relative to volume energies. However, with this increase in system size there would be a similar increase in computation time. The standard way of overcoming this problem is the use of periodic boundary conditions (pbcs). In this method, which is similar to the pbcs employed in field theory [MS84], images of the system are placed all around the primary cell. Particles which move through one face of the cell are replaced by their

images coming through the opposite face, for example in Fig. 3.4 particle 1 leaving the right side of the simulation cell is replaced by particle 1' coming from the left image cell.

This takes care of point particle movements. In calculating pair potentials and forces the minimum image convention (MIC) is used and particles only interact with the closest image of other particles. Again referring to Fig. 3.4 and the interaction between particle 2 and 3, the interaction would actually be calculated by using the distance between particle 2 and 3', because particle 3' is closer to 2 than 3. In the current case, point particles will only interact with one image of other particles and will not interact with themselves as long as the minimum box dimension is at least twice the cut-off radius of the pair potential used. This method of periodic boundary conditions ensures that the system remains homogeneous.

The above example is well known and standard in the description of periodic boundary conditions for molecular dynamics simulations. What is not so well known is that these boundary conditions are equivalent to spatio-temporal mappings. A map is an operation that transforms the state of a system at time t to an allowable state at time $t + 1$. Maps have been particularly instrumental in our understanding of chaos in dynamical systems in recent years. A functional mapping may be defined as

$$\mathbf{x}_{t+1} = M(\mathbf{x}_t) \tag{3.30}$$

where \mathbf{x} is an n -dimensional vector that describes the state of the system and M is the mapping operation. For the case of an equilibrium MD system, such a mapping scheme for particle positions is

$$\begin{pmatrix} x' \\ y' \\ z' \end{pmatrix} = \begin{pmatrix} 1 & 0 & 0 \\ 0 & 1 & 0 \\ 0 & 0 & 1 \end{pmatrix} \begin{pmatrix} x \\ y \\ z \end{pmatrix} \text{mod}(L) \tag{3.31}$$

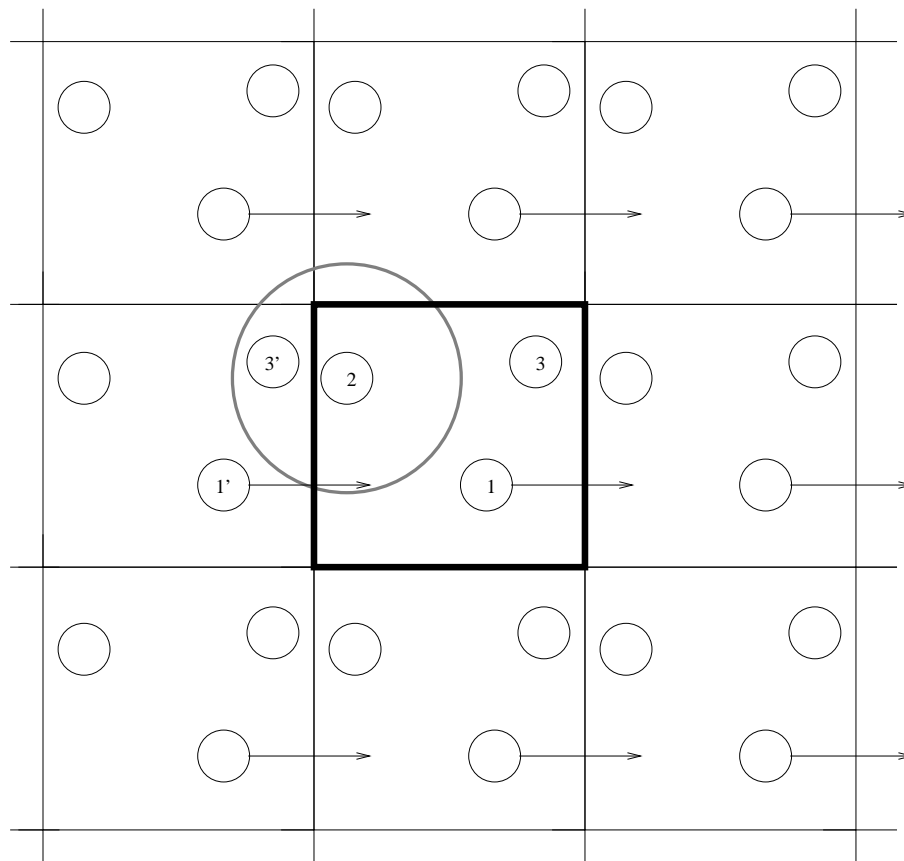


Figure 3.4: The square periodic boundary conditions commonly used for equilibrium molecular dynamics simulations. The central cell (bold) is the primary cell and the cells surrounding it are its periodic images. Particles 1' and 3' are periodic images of particle 1 and 3, respectively. Due to the minimum image convention atom 2 interacts with particle 3' and not particle 3. The large circle has a radius twice the cut-off radius.

where L is the length of the simulation cell.

Notice that the physical mapping of a particle with coordinates $\mathbf{x} = (x, y, z)$ into one with coordinates $\mathbf{x}' = (x', y', z')$ occurs due to the modulo operation. Only when particles move out of the simulation cell does the modulo operation map these particles back into the cell; otherwise particle positions remain unchanged by the mapping. The mapping operation described in (3.31) is thus equivalent to the scheme of periodic boundary conditions used in a typical equilibrium MD simulation.

Two alternative ways of describing these periodic boundary conditions using the notions of topology are as the quotient space $\mathbb{R}^3/\mathbb{Z}^3$ or as a product space $\mathbb{T}^3 = \mathbb{S}^0 \times \mathbb{S}^0 \times \mathbb{S}^0$, where \mathbb{S}^0 is a circle. In these representations particles are restricted to move in a space with the designated topology. We have chosen to use the map (3.31) because it follows the style of the algorithm used to actually simulate the system. Further theoretical developments may benefit from using alternative descriptions. The quotient space description has been emphasised in a recent work by Sausset and Tarjus [ST07].

3.6.2 Shear flow

For simulations of PCF the boundary conditions are no longer stationary but become periodic in time. In the Lees-Edwards scheme of periodic boundary conditions [LE72] shown in Fig. 3.5, periodic images above the primary cell slide with velocity $+\dot{\gamma}L$ while the images below slide with velocity $-\dot{\gamma}L$. The initial condition of the system of cell and images is the stationary periodic boundary conditions for the simulation of an equilibrium system. Now because of the motion of the cells above and below the primary cell, the x component of the position of a particle must be adjusted by an amount $\pm\dot{\gamma}L\Delta t$, where Δt is the integration time step. For example, if particle 2 moves through the bottom interface, it re-emerges shifted by an amount $-\dot{\gamma}L\Delta t$ in the $\hat{\mathbf{n}}_x$ direction. The periodic boundary conditions described above are termed ‘sliding brick’ pbcs.

An equivalent representation is the Lagrangian-Rhomboid scheme [Eva79]. In this scheme the simulation cell deforms with the flow so that if the initial simulation cell is the cube $(x, y, z)^T \in [0, L] \times [0, L] \times [0, L]$ then at time t

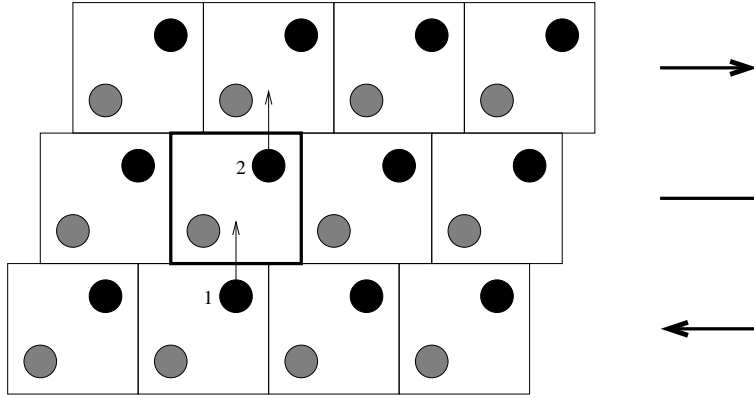


Figure 3.5: Lees-Edwards ‘sliding brick’ periodic boundary conditions for planar Couette flow. When particle 2 moves out of the top of the central cell (bold) it re-emerges through the bottom of the cell shifted horizontally by an amount $-\dot{\gamma}L\Delta t$.

the primary cell is given by

$$\begin{pmatrix} x' \\ y' \\ z' \end{pmatrix} = \begin{pmatrix} 1 & \dot{\gamma}t & 0 \\ 0 & 1 & 0 \\ 0 & 0 & 1 \end{pmatrix} \begin{pmatrix} x \\ y \\ z \end{pmatrix} \quad (3.32)$$

An instantaneous configuration of the cell and its periodic images is given in Fig. 3.6. If τ_p is the time period of the mapping, then at time $t = \tau_p = 1/\dot{\gamma}$ the cell is mapped back to the original cell. As in the case of the equilibrium mapping, this *nonequilibrium* mapping is achieved by using the modulo operation. Between $t = 0$ and $t = \tau_p$ the overall displacement of particles due to the streaming velocity is given by the map

$$\begin{pmatrix} x' \\ y' \end{pmatrix} = \begin{pmatrix} 1 & 1 \\ 0 & 1 \end{pmatrix} \begin{pmatrix} x \\ y \end{pmatrix} \text{mod}(L) \quad (3.33)$$

where we note that as there is no flow in the $\hat{\mathbf{n}}_z$ direction the nonequilibrium subset of the complete three-dimensional mapping need only be described by a two dimensional matrix. Note that even though there is no flow in the

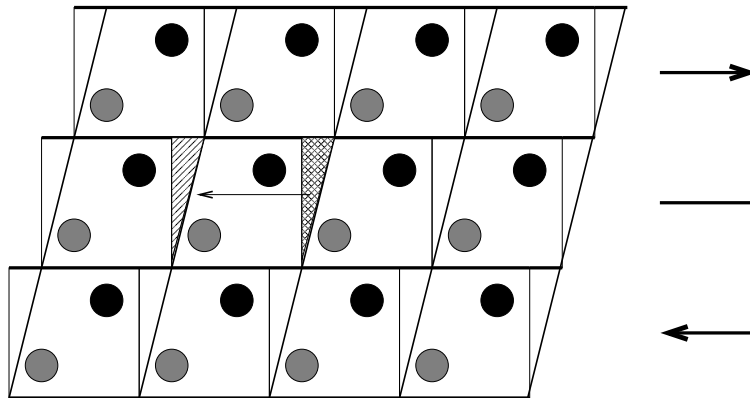


Figure 3.6: The Lagrangian-Rhomboid scheme for NEMD simulations of planar Couette flow. The equivalence of this scheme with the sliding brick scheme of Fig. 3.5 can be seen by removing the right cross-hatched triangular section from the primary cell, shifting it by an amount $-L$ in the horizontal direction, and re-inserting it into the left striped triangular section. Both schemes preserve the relative spatial separations between all particles exactly.

\hat{n}_y direction, the y coordinate *does* appear in the mapped x coordinate (*i.e.* x'). This mapping is depicted in Fig. 3.7 with regions shaded to show how they transform.

An important feature of (3.33) to note is that the transformed cell maps exactly over the original cell. The boundary conditions for PCF are thus not only spatially periodic but also periodic in time. It is also of note that molecular dynamics simulations that utilise such spatio-temporal periodic boundary conditions are actually non-autonomous [PE98] (*i.e.* their motion depends on t explicitly); as such there is no way which any simulation of this type can be truly ‘steady-state’. For most simulations of this sort, however, the system size is sufficiently large that the time and space periodicity inherent in the periodic boundary conditions is negligible.

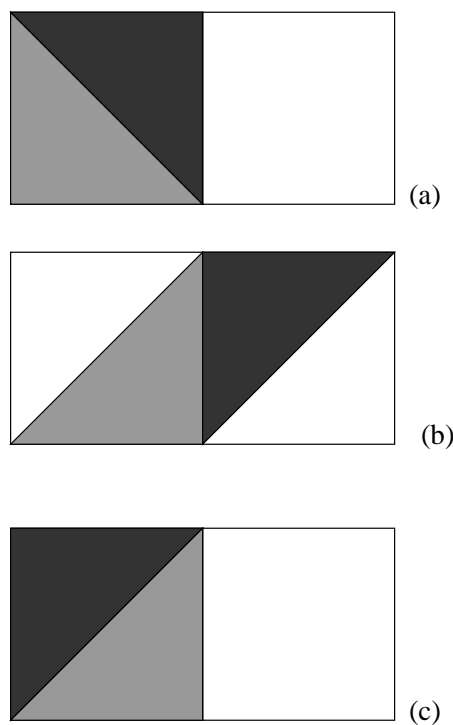


Figure 3.7: A diagram of the map used with Lagrangian-Rhomboid periodic boundary conditions in molecular dynamics simulations of planar Couette flow. Shading distinguishes different regions of the map for clarity of visualisation. (a) The initial configuration of the map, in the unit square. (b) The transformed map. (c) The transformed region is mapped back into the unit square.

3.6.3 Extensional flow

The pbc's we use to simulate PEF were developed by Kraynik and Reinelt for use in the simulation of multi-phase flow [KR92] and implemented for molecular dynamics by Todd and Daivis [TD98, TD99] and independently by Baranyai and Cummings [BC99]. The analysis of Kraynik and Reinelt showed that it would be impossible to create a similar type of pbc based on a so called reproducible lattice for either uniaxial or biaxial extension. Analysis in Appendix 1 discusses how the method of Kraynik and Reinelt might be generalised to planar mixed flow *i.e.* flow with both planar shear and planar extensional components. The Kraynik Reinelt pbc's are both spatially and

temporally periodic. By rotating a square lattice to a “magic angle” and performing elongation with respect to the original lattice it was shown that after a period τ_p the lattice can be reproduced onto the original lattice, so that the final configuration can be mapped back to the original lattice and the simulation can continue.

Some care needs to be taken in implementing this method. Todd and Daivis [TD00] later found that exponential growth in the total centre of mass momentum due to numerical round off leads to a similar growth in the kinetic energy, and hence kinetic temperature which after a time could not be compensated for by the thermostat. They found that this deviation could be overcome by rescaling the momenta periodically and/or using a dynamical constraint mechanism so that the centre of mass momentum was conserved. We have adopted their method in our simulations and have encountered no unexpected deviations in the kinetic temperature of the system. We have also used both the Lagrangian-Rhomboid boundary conditions implemented by Todd and Daivis and the neighbour list together with the cell method developed by Matin *et al.* [MDT03].

Given the equations of motion it is necessary to find a suitable set of pbcs. Simple cubic periodic boundary conditions aligned parallel with the directions of expansion and contraction are severely limited because ultimately the simulation must cease once the length of the cell in the contracting direction reaches its minimum extension of twice the range of the interatomic potential radius.

Kraynik and Reinelt [KR92] demonstrated how the extensional motion of spatially periodic lattices could be generated by suitable geometric orientations of the axes of the lattice with respect to the orientation of the extensional field. As described in [TD98, TD99, BC99], such periodic lattices may be used as the boundaries of a periodic simulation cell. In their derivation Kraynik and Reinelt [KR92] first construct an arbitrary lattice

consisting of points $\mathbf{L}_i(t)$ governed by the dynamical equation

$$\mathbf{L}_i(t) = \mathbf{N}(t) \cdot \mathbf{L}_i(0) \quad (3.34)$$

$$= N_{i1}(t)\mathbf{L}_1(0) + N_{i2}(t)\mathbf{L}_2(0) + N_{i3}(t)\mathbf{L}_3(0) \quad (3.35)$$

$\mathbf{L}_i(0)$ are the initial linearly independent basis lattice vectors, $\mathbf{N}(t) = \exp(\nabla\mathbf{u}t)$ is the matrix that describes the evolution with time of these basis vectors, $\nabla\mathbf{u}$ is the strain rate tensor and \mathbf{u} is the streaming fluid velocity. For a lattice to be reproducible (*i.e.* periodic in space and time), the constants $N_{ij}(t)$ must be integers at some time $t = \tau_p$. Kraynik and Reinelt then determined which set of integers $N_{ij}(\tau_p)$ make (3.34) valid for a variety of extensional flows described by $\nabla\mathbf{u}$. These integers define the mapping, hereafter termed the K-R map. In turn, this reduces to the solution of an eigenvalue problem with corresponding eigenvectors. For the case of PEF, described by

$$\nabla\mathbf{u} = \begin{pmatrix} \dot{\epsilon} & 0 & 0 \\ 0 & -\dot{\epsilon} & 0 \\ 0 & 0 & 0 \end{pmatrix}. \quad (3.36)$$

The eigenvalues were shown to be

$$\lambda_1 = \frac{k + (k^2 - 4)^{1/2}}{2}; \lambda_2 = \lambda_1^{-1} = \frac{k - (k^2 - 4)^{1/2}}{2} \quad (3.37)$$

where k is an integer with allowable values $k \geq 3$. Note that not all values of k are allowed, although there are an infinite number of them.

The directions of the two orthogonal eigenvectors (\mathbf{e}_1 and \mathbf{e}_2) in turn define the directions of the expanding and compressing fields with respect to the orientation of the basis vectors of the square lattice. If the x axis is chosen in the direction of expansion (at a rate $\dot{\epsilon}$), and the y axis is thus the direction of compression (at a rate $\dot{\epsilon}$), then the angle between \mathbf{e}_1 (parallel to the x axis) and the lattice basis vector \mathbf{b}_1 is the orientation angle θ

(see Fig. 3.8 as well as Fig. 1 in [TD98] and A-1 in Appendix 1). There are an infinite number of these ‘magic’ angles which the initial lattice (or, equivalently, simulation cell) can be aligned with respect to the flow fields that guarantees the simulation cell is infinitely periodic in both space and time.

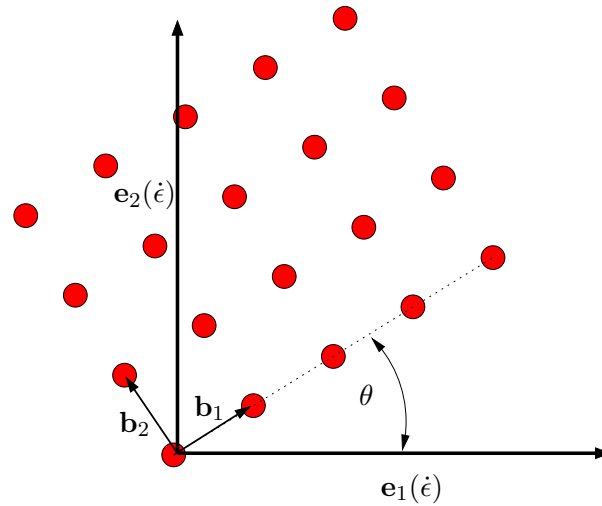


Figure 3.8: Alignment of lattice basis vectors \mathbf{b}_1 and \mathbf{b}_2 with eigenvectors \mathbf{e}_1 and \mathbf{e}_2 as performed in our NEMD simulations. The vector \mathbf{e}_1 is the direction of extension ($\dot{\epsilon}$), while \mathbf{e}_2 is the direction of compression ($-\dot{\epsilon}$). The orientation angle θ is the angle between \mathbf{e}_1 and \mathbf{b}_1 .

As demonstrated above in the discussion of pbcs for shear flow, it is this spatio-temporal periodicity, coupled with the SLLOD equations of motion, which allows one to perform NEMD simulations of spatially homogeneous flow indefinitely. If τ_p is the lattice strain period, then the actual mapping of the extended simulation cell back into its original cell shape occurs when the value of the strain, $\epsilon = \dot{\epsilon}\tau_p$ equals the Hencky strain [KR92], ϵ_p .

The original derivation of the eigenvalues, eigenvectors and orientation angles, while complete, is algebraically involved. In fact, Kraynik and Reinelt [KR92] assist readers with tables of orientation angles and relevant matrices of integers $N_{ij}(\tau_p)$ for square (up to $k = 51$) and hexagonal (up to $k = 148$) lattices undergoing planar extensional flow. In the next section, we

show how these periodic lattices are directly related to the Arnold cat map, and demonstrate a simplified approach to compute the eigenvectors and orientation angles.

3.7 The Arnold cat map and Kraynik-Reinelt boundary conditions

The usual Arnold cat map [AA68] of the torus $\mathbb{T}^2 = \mathbb{R}^2/\mathbb{Z}^2$ onto itself is given by

$$\begin{pmatrix} x' \\ y' \end{pmatrix} = \begin{pmatrix} 1 & 1 \\ 1 & 2 \end{pmatrix} \begin{pmatrix} x \\ y \end{pmatrix} \text{ mod}(1). \quad (3.38)$$

In this representation of the cat map, expansion takes place in the direction of the eigenvector \mathbf{e}_1 and contraction occurs in the direction of the eigenvector \mathbf{e}_2 (see Fig. 3.9). Thus the cat map ‘flow’ geometry is the opposite of the flow geometry employed by Kraynik and Reinelt and subsequent NEMD simulations of planar elongational flow [TD98, TD99, BC99].

The map described by (3.38) has two eigenvalues,

$$\lambda_1 = \frac{3 + \sqrt{5}}{2} > 1, \quad \lambda_1^{-1} = \lambda_2 = \frac{3 - \sqrt{5}}{2} < 1. \quad (3.39)$$

The eigenvalues are equivalent to those found by Kraynik and Reinelt, whose general solution is given in (3.37). Eqn. (3.39) is satisfied for $k = 3$ in (3.37). For the cat map, this corresponds to an alignment of the direction of expansion (in this case, parallel to the eigenvector, \mathbf{e}_1) at an angle $\theta = 31.7^\circ$ with respect to the y axis (equivalent to the angle formed between \mathbf{e}_2 and the x axis). Any other allowable values of k may be used, and as previously noted there are an infinite number of them. They in turn correspond to the hyperbolic toral automorphisms, which in turn are a set of Anosov diffeomorphisms [KH95]. Since the map is area preserving, the product of any set

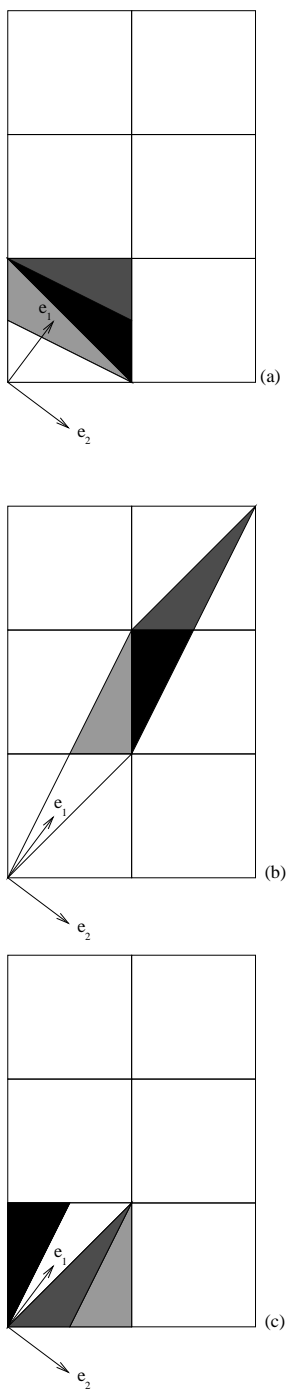


Figure 3.9: A diagram of the usual Arnold cat map. The vectors e_1 and e_2 give the expanding and contracting directions of the map for clarity of visualisation. (a) The initial configuration of the map, in the unit square. (b) The transformed map. (c) The transformed region is mapped back to the unit square.

of eigenvalues is 1. The eigenvectors of the map described by (3.38) are

$$\mathbf{e}_1 = \begin{pmatrix} s \\ \frac{\sqrt{5}+1}{2}s \end{pmatrix}, \mathbf{e}_2 = \begin{pmatrix} s \\ \frac{-\sqrt{5}+1}{2}s \end{pmatrix}, \quad (3.40)$$

where s is a real number. For convenience we set $s = 1$.

We note here that the Arnold cat map transformation is equivalent to the mapping that takes place in the Kraynik-Reinelt lattice when the Hencky strain, $\epsilon_p = \dot{\epsilon}\tau_p$, is attained, and we have already noted that it is this mapping which makes the Kraynik-Reinelt system reproducible, and hence periodic in time as well as space.

We give a digram of the map described by (3.38) in Fig. 3.9. The relevant region starts as a unit square, Fig. 3.9(a), and is transformed to a parallelogram, Fig. 3.9(b), under the action of the integer matrix. The action of the modulo operation maps the transformed region back to the unit square, Fig. 3.9(c). Alternatively, one can view the modulo operation as being inherently due to the periodicity of the torus. The shading in the diagram helps to show how different regions transform.

The example given in (3.38) is not a unique example of this type of map. The matrix in (3.38) can be replaced by any integer matrix with non-unit eigenvalues and positive or negative unit determinant. These maps are known as hyperbolic toral automorphisms, which in turn are a set of Anosov diffeomorphisms [KH95]. The family of lattices found by Kraynik and Reinelt [KR92] corresponds to a subset of hyperbolic toral automorphisms. The simplest of these and the one chosen for the molecular dynamics simulations discussed earlier, is

$$\begin{pmatrix} x' \\ y' \end{pmatrix} = \begin{pmatrix} 2 & -1 \\ -1 & 1 \end{pmatrix} \begin{pmatrix} x \\ y \end{pmatrix} \text{mod}(1). \quad (3.41)$$

This map is depicted in Fig. 3.10 and again areas are shaded to show how

they transform. The eigenvalues of this map are the same as those of the usual Arnold cat map, while the eigenvectors are swapped, making this map the inverse of the cat map. This can be observed by inspecting the initial and final configurations of the two maps shown in Figs. 3.9 and 3.10. At the beginning of the NEMD simulations the cell is rotated so that the extension and compression axes align with the x and y axes respectively [TD98, TD99].

We now demonstrate that it is far simpler to compute the eigenvalues, eigenvectors and orientation angles from the cat map formalism, rather than the method employed by Kraynik and Reinelt [KR92]. Consider the set of Anosov diffeomorphisms with the mapping

$$\mathbf{x}' = \mathbf{M}(\mathbf{x}) \quad (3.42)$$

where

$$\mathbf{M} = \begin{pmatrix} m_1 & m_2 \\ m_2 & m_3 \end{pmatrix} \quad (3.43)$$

is symmetric and $m_1, m_2, m_3 \in \mathbb{Z}$. These mappings are characterised by integer matrix elements and have the constraint imposed on them so that they are area preserving, *i.e.*

$$\det(\mathbf{M}) = m_1 m_3 - m_2^2 = \pm 1. \quad (3.44)$$

In this work we do not consider the $\det(\mathbf{M}) = -1$ case, since it corresponds to a mapping which does not preserve the orientation of the mapped region and is therefore not useful for simulations. The eigenvalue equation for the map (3.42) is

$$\det(\lambda \mathbf{I} - \mathbf{M}) = 0, \quad (3.45)$$

which when solved on substitution in (3.45) for the case $\det(\mathbf{M}) = +1$, gives

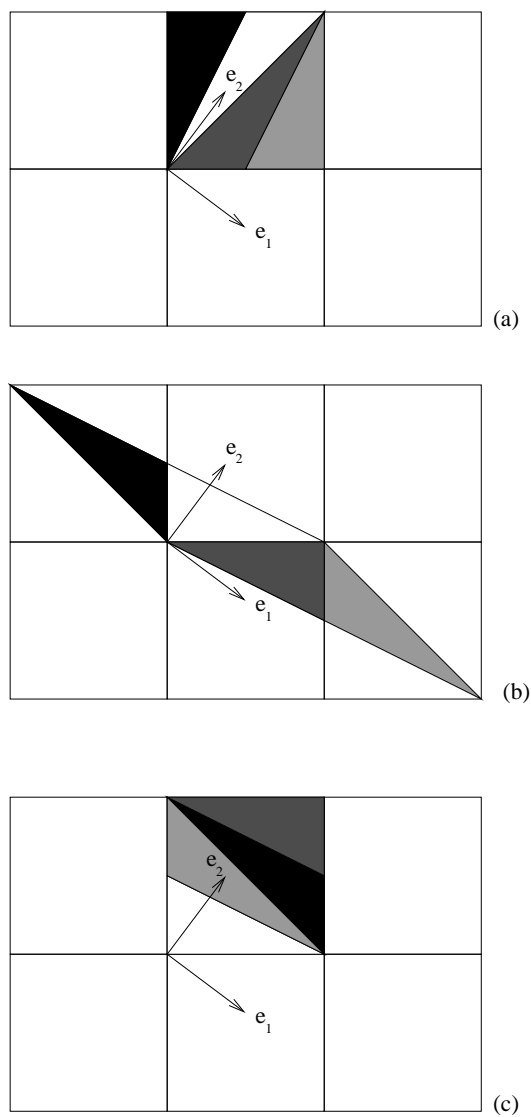


Figure 3.10: A diagram of the Kraynik-Reinelt map used in molecular dynamics simulations. The vectors \mathbf{e}_1 and \mathbf{e}_2 give the expanding and contracting directions of the map respectively. Shading represents different regions of the map for clarity of visualisation. (a) The initial configuration of the map, in the unit square. (b) The transformed map. (c) The transformed region is mapped back to the unit square.

the pair of eigenvalues

$$\lambda = \frac{(m_1 + m_2) \pm \sqrt{(m_1 + m_2)^2 - 4}}{2} \quad (3.46)$$

Comparison with (3.37) for the Kraynik-Reinelt map shows that $k = \text{trace}(\mathbf{M})$. The Hencky strain is simply computed as $\epsilon_p = \log_e(\lambda)$ [KR92].

The eigenvectors of \mathbf{M} may now be trivially computed from the set of linear equations,

$$\mathbf{M}\mathbf{x} = \lambda\mathbf{x} \quad (3.47)$$

giving us

$$\mathbf{e}_1 = \begin{pmatrix} s \\ \frac{(\lambda_1 - m_1)}{m_2} s \end{pmatrix}, \mathbf{e}_2 = \begin{pmatrix} s \\ \frac{(\lambda_2 - m_1)}{m_2} s \end{pmatrix} \quad (3.48)$$

Once again, we set $s = 1$ for convenience. We note that $m_2 = 0$ does not correspond to an Anosov diffeomorphism.

We denote the unit vector in the x direction as $\hat{\mathbf{n}}_x$ for the flow geometry adopted in Fig. 3.10. The orientation angle (*i.e.* the angle between the expanding direction and the x axis) can be thus simply computed from

$$\mathbf{e}_1 \cdot \hat{\mathbf{n}}_x = \|\mathbf{e}_1\| \|\hat{\mathbf{n}}_x\| \cos \theta \quad (3.49)$$

i.e.

$$\theta = \cos^{-1} \left(\frac{\mathbf{e}_1 \cdot \hat{\mathbf{n}}_x}{\|\mathbf{e}_1\|} \right) \quad (3.50)$$

In fact it is clear that the matrix elements $N_{11}(\tau_p), N_{12}(\tau_p), N_{21}(\tau_p)$ and $N_{22}(\tau_p)$ in the K-R map are equivalent to m_3, m_2, m_2 and m_1 , respectively. However, our derivation of the eigenvalues, eigenvectors and orientation angles is somewhat more straightforward and simpler than that worked out in [KR92]. In particular, it is the orientation angle and Hencky strain (hence, strain period) that are of central importance in the practical implementation of the K-R map in NEMD simulations [TD98, TD99].

As an example, consider the map

$$\mathbf{M} = \begin{pmatrix} 5 & -2 \\ -2 & 1 \end{pmatrix} \quad (3.51)$$

It has eigenvalues $\lambda = 3 \pm 2(\sqrt{2})$ and eigenvectors

$$\mathbf{e}_1 = \begin{pmatrix} 1 \\ 1 - \sqrt{2} \end{pmatrix} \quad (3.52)$$

and

$$\mathbf{e}_2 = \begin{pmatrix} 1 \\ 1 + \sqrt{2} \end{pmatrix} \quad (3.53)$$

The Hencky strain ($\ln \lambda$) is thus 1.76275 and the orientation angle (from (3.50) is $\theta = 22.5^\circ$. Use of the cat map formalism determines these useful quantities in several lines of trivial algebra, compared to pages of algebra following the Kraynik-Reinelt procedure.

Three iterations of Arnold cat map are shown in Fig. 3.11. Already at the third iteration we see that the original region of the cat face is being dispersed over the entire region $[0, 1] \times [0, 1]$. This is known as ergodic behaviour. With analogs found in many dynamical systems the ergodic property has central importance in statistical mechanics. The image appears in bands aligned with the eigenvector corresponding to the positive eigenvalue of the map, *i.e.* the extensional direction of the map.

Despite the ergodic nature of the cat map, it can be shown [KH95] that the rational points

$$\begin{pmatrix} \frac{p}{q} \\ \frac{r}{s} \end{pmatrix}; p, q, r, s \in \mathbb{Z} \quad (3.54)$$

are periodic, and while this may induce artificial correlations when simulating a solid, correlations are unlikely to be noticeable when dealing with a fluid system which even at equilibrium has a relatively short correlation

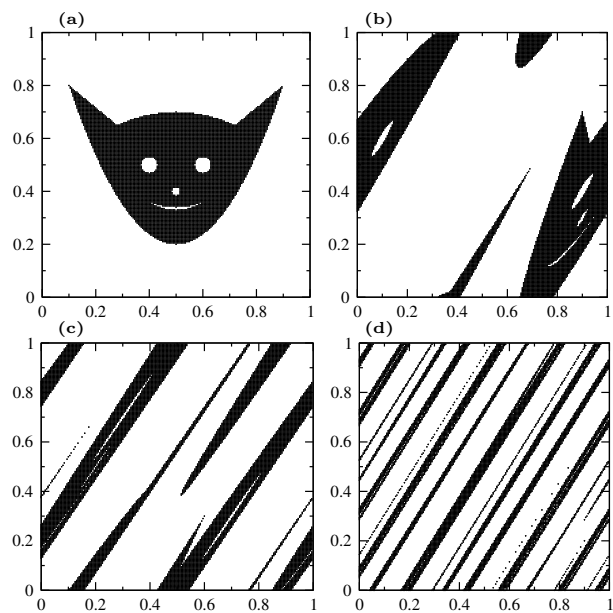


Figure 3.11: The Arnold cat map. (a) The initial configuration of the map shows the picture of a cat's face. (b) The first iteration of the cat map (3.38). After one iteration, it can be seen that the eyes which were originally circular have been deformed into ellipses. (c) The second iteration of the cat map. (d) The third iteration of the cat map. After three iterations of the map, points have been dispersed in fairly even bands over the unit square.

time.

In a further investigation [TD00] it was found that the use of Kraynik-Reinelt periodic boundary conditions was inherently unstable for very long simulations, and that momentum was not conserved in the direction of contraction. The total linear momentum in the contracting direction was found to grow exponentially with time, leading to a catastrophic failure of the algorithm at long times. This exponential growth was due to numerical imprecision in the zeroing of the initial momentum necessary for conservation of momentum to prevail at all times. To counter this it was demonstrated [TD00] that one could either use a constraint mechanism to keep the total momentum constant, or alternatively one could periodically zero the centre-of-mass momentum. The source of this instability is equivalent to that described (for example) by McCauley [McC97] who, in his discussion of the Arnold cat map, points out that when simulating the Arnold cat map on a computer, numerical accuracy decreases exponentially with each application of the map. The implication is that for highly accurate results one is required to deal with numbers with many decimal places, and that the degree of accuracy is limited by the length of the simulation desired (*i.e.* the number of iterations required).

Since the work on the stability of SLLOD under PEF by Todd and Daivis [TD00], there has been considerable interest in the chaotic properties of these systems. In particular the Lyapunov exponents [Ott02, EM90], an important measure of the chaotic nature of dynamical systems, have been investigated. Todd [Tod05] made the observation that the Lyapunov exponents for the streaming part of the flow are the eigenvalues of the associated map. Frascoli *et al.* [FST06] have investigated the chaotic properties of atomic systems under PEF and compared them with properties under PCF. In particular they have calculated the Lyapunov exponents and showed that under PEF these exponents obey the conjugate pairing rule. Their reexamination of the

Lyapunov exponents for PCF under SLLOD dynamics with the Gaussian isokinetic-kinetic thermostat has provided evidence that the conjugate pairing rule is not obeyed for this system. Following this investigation Frascoli *et al.* [FTS07] have shown that the spectrum of Lyapunov exponents for PEF is independent of the choice of K-R pbc's used for the simulation. We noted above that these authors have also developed simulations of PEF at constant pressure [FT07] and these methods have also been used to compare the Lyapunov exponents under PEF for these systems with those at constant volume [FST].

Recent works [PJ03, JP04, vZ99] have simulated systems of hard spheres and disks under PCF using SLLOD and using the colour conductivity algorithm. These simulations have relied on the analytic solution of the trajectories between collisions. In the work of Petravac and Jepps [PJ03] it was found that the dynamics at collisions was independent of the applied field. We have performed a similar calculation for systems under PEF finding analytic solutions to the trajectory of particles between collisions. We suggest that, in light of the simplified particle interactions for systems of hard spheres and the success of previous works under PCF by Petravac *et al.* [PIM94, PI95] of small numbers of particles, similar simulations under PEF using analytic solutions for trajectories may give further insight into any influence of the cat map on the dynamics.

Settings of dynamical systems in the complex plane can often be enlightening. Recently, for example, the Lorentz gas – a prototypical billiard system – has been investigated in the complex plane by Barra and Gilbert [BG07] following from work by Wojkowski [Woj00]. We wish to make a few tentative observations with regard to possible complex settings of n-body dynamics: One could analyse a system of interacting particles by using the elliptic functions [Lan99] which have inherent periodicity of a two-dimensional lattice in the complex plane. The type of interaction induced between particles by

the elliptic functions already have application in the field of two-dimensional fluid mechanics where the motion of vortex-centres obey Hamilton's equations with a logarithmic pair potential [O'N89, MP94, Bat67]. The Weierstrass elliptic function is also used as the pair potential between particles in the Calogero-Moser system [Mos75, BBT03], an integrable n-body system of particles constrained to one dimension. If one were to transfer PCF and PEF to the complex plane, a complex equivalent to the pbc maps we described above is required. For the two specific examples (3.33) and (3.38) the corresponding complex maps are,

$$f_{PCF}(z) = \frac{1}{2}[(2-i)z - i\bar{z}] \quad (3.55)$$

$$f_{PEF}(z) = \frac{1}{2}[3z - (1+2i)\bar{z}] \quad (3.56)$$

Both of these functions contain the complex conjugate \bar{z} of z and thus neither corresponds to a conformal map. These functions are however, *quasiconformal* as defined for example by Ahlfors [Ahl06].